White Rose Research Online

eprints@whiterose.ac.uk
https://eprints.whiterose.ac.uk
Universities of Leeds, Sheffield and York

Deposited via The University of York.

White Rose Research Online URL for this paper:
https://eprints.whiterose.ac.uk/id/eprint/165909/

Version: Submitted Version

Article:
Dudson, Benjamin Daniel, Gracias, W A, Jorge, Rogerio et al. (2021) Edge turbulence in ISTTOK: a multi-code fluid validation. Plasma Physics and Controlled Fusion. 055013. ISSN: 1361-6587

https://doi.org/10.1088/1361-6587/abe21d

Reuse
Items deposited in White Rose Research Online are protected by copyright, with all rights reserved unless indicated otherwise. They may be downloaded and/or printed for private study, or other acts as permitted by national copyright laws. The publisher or other rights holders may allow further reproduction and re-use of the full text version. This is indicated by the licence information on the White Rose Research Online record for the item.

Takedown
If you consider content in White Rose Research Online to be in breach of UK law, please notify us by emailing eprints@whiterose.ac.uk including the URL of the record and the reason for the withdrawal request.

UNIVERSITY OF LEEDS
University of Sheffield
UNIVERSITY of York

Edge turbulence in ISTTOK: a multi-code fluid validation

B. D. Dudson[1], W. A. Gracias[2], R. Jorge[3,4], A. H. Nielsen[5], J. M. B. Olsen[5], P. Ricci[3], C. Silva[4], P. Tamain[6], G. Ciraolo[6], N. Fedorczak[6], D. Galassi[3,7], J. Madsen[5], F. Militello[8], N. Nace[6], J. J. Rasmussen[5], F. Riva[3,8], E. Serre[7]

[1]York Plasma Institute, Department of Physics, University of York YO10 5DQ, UK
[2]Universidad Carlos III de Madrid, Leganés, 28911, Madrid, Spain
[3]École Polytechnique Fédérale de Lausanne (EPFL), Swiss Plasma Center (SPC), CH-1015 Lausanne, Switzerland
[4]Instituto de Plasmas e Fusão Nuclear, Instituto Superior Técnico, Universidade de Lisboa, 1049-001 Lisboa, Portugal
[5]Department of Physics, Technical University of Denmark, Fysikvej, DK-2800 Kgs.-Lyngby, Denmark
[6]IFRM, CEA Cadarache, F-13108 St. Paul-lez-Durance, France
[7]Aix Marseille Univ, CNRS, Centrale Marseille, M2P2 Marseille, France
[8]CCFE, Culham Science Centre, Abingdon, Oxon, OX14 3DB, United Kingdom

E-mail: `benjamin.dudson@york.ac.uk`

Abstract. Fluid models used to study the edge plasma region need to be benchmarked against similar conditions given that models can strongly differ in complexity and therefore the results they produce. Via this validation study undertaken through the framework of EUROfusion Enabling Research, four state-of-the art models - GBS, Hermes/BOUT++, HESEL and TOKAM3X - are compared to experimental plasma turbulence measurements on the ISTTOK tokamak. Statistical comparisons of simulation and experiment data show that fluid models used here can replicate most of the experiment in terms of I_{sat} and V_{float} fluctuations. Furthermore, it is shown that without including more complex information (like core turbulence information and domain geometry details and magnetic topological aspects) in fluid models, the results recovered can fall short from the experimental results. Via the simulations using these codes, it is demonstrated that fluid models continue to be a good cost-effective tool in recovering many global aspects of edge plasma behaviour.

Submitted to: *Plasma Phys. Control. Fusion*

1. Introduction

The scrape-off layer (SOL) of magnetically confined plasmas is where the hot core meets material surfaces [1], and is crucial to the design and operation of high power devices whilst keeping heat loads to the walls within acceptable technological limits (typically around 10 MW/m^2) and restricting high-Z impurities sputtered from walls into the core plasma. As fusion devices get better in performance, as is the aim with ITER, the power fluxes in the SOL become larger making the safe handling of these fluxes important for the success of such devices as future power plants [2].

Most current tokamak designs and projections are based on extrapolation from experimental data [3], with some theoretical support [4], but are not completely understood. Therefore the modelling of the turbulence and transport in these devices has a crucial role to play in calculating fluxes and then testing the limits of validity of the experimental scalings obtained. This will enable in the understanding of the underlying physical mechanisms in turbulence, and in the identifying where there may be changes of regimes, or totally novel effects coming into play that were not accounted for in the models. In order to be able to do this, the models used must first be validated against existing experiments so that the strengths and limitations of these models in reproducing experimental conditions are understood.

In recent years a programme of thorough code verification and validation has been undertaken under EUROFusion project CfP-WP15-ENR-01/EPFL-05, to characterise and improve our predictive capability in simulating the edge of tokamak plasmas. This has included verification that the codes solve the analytic equations faithfully [5, 6, 7], and validation of individual blob dynamics in TORPEX [8] and MAST [9]. In the same vein, this work is extended here via a code validation exercise, comparing fluctuation characteristics from the ISTTOK tokamak to simulations using the same codes used in the previously cited validation studies (i.e. GBS [10, 11], Hermes/BOUT++ [12, 13], HESEL [14] and TOKAM3X [15, 7] codes). All codes are based on drift-reduced collisional fluid models [16], differing in their choice of terms retained in the models, coordinate systems used, and numerical methods implemented. This work extends previous simulations of ISTTOK using GBS [17], where profiles of statistical moments (mean, standard deviation, skewness and kurtosis) were found to be in generally good agreement with experimental data. Those simulations did not however reproduce large intermittent events seen experimentally in the near SOL. A possible cause of this was identified as dynamics in the core plasma, which was not included in the model. Here all simulations include both core (closed field-line) and SOL (open field-line) regions and an attempt is made at comparing simulations with the experiment, to identify the impact of the differences between individual numeric models on the results obtained.

Section 2 describes the experimental data, including details of the location and response characteristics of the probe diagnostics, followed by brief descriptions of the simulation codes used herein (full details of the codes in the references cited). Experimental and simulated data are then compared in section 3 in terms of their

statistics and radial profiles (section 3.1), probability density functions (section 3.2) and Fourier power spectral density (section 3.3). The turbulence simulations performed here do not include the segmented structure of the poloidal limiter in ISTTOK. So in section 4.1 the TOKAM3X code is used to assess the importance of this segmented structure. Finally in section 5 we draw conclusions and make suggestions for further work.

2. Experimental details and numeric models used

2.1. ISTTOK experimental data

Measurements were carried out for a H-plasma in the large aspect ratio circular cross-section tokamak ISTTOK, which has a major radius of $R = 0.46\,\mathrm{m}$, minor radius of $a = 0.085\,\mathrm{m}$, vessel minor radius $a_{vessel} = 0.1\,\mathrm{m}$, toroidal magnetic field of $B_T = 0.5\,\mathrm{T}$, plasma current of $I_p = 4 - 6\,\mathrm{kA}$ and an line-averaged density of $\bar{n} = 3 - 5 \times 10^{19}\,\mathrm{m}^{-3}$. The experimental data and simulations shown here employ a safety factor $q = 8$ at the separatrix.

ISTTOK has a poloidal graphite limiter that is electrically connected to the vessel. The limiter is shown in figure 1 and is segmented, being composed of 12 equally sized rectangular blocks of poloidal extent of about 25 mm and equidistant from each other. The shape of this limiter, in practice, results in a significant variation (by a factor of two) in the parallel connection length in the poloidal plane depending on its poloidal angle location. But in the simulated cases, the limiter is considered to be continuous as against segmented so as to be able to attribute any differences in results to the underlying models alone. The impact of the limiter's true geometry over and above the effects of each model on plasma profiles is the subject of the discussion in section 4.1.

Around the limiter radius the electron temperature and ion temperature are about $T_e \approx T_i \approx 20\,eV$ and the electron density $\approx 10^{18}\,m^{-3}$. The ion Larmor radius is approximately $\rho_s \simeq 0.9$ mm. These plasma parameters give a collision time $\tau_e \simeq 2.3\,\mu$s, electron mean free path of $\lambda_e \simeq 4.3$m and ion mean free path of $\lambda_i \simeq 6.1$m. These are comparable to the connection length $L_{||} \simeq 3-6$m along the magnetic field in the SOL of ISTTOK. All simulations shown here use drift-ordered fluid equations with collisional closures for the higher order moments. The limitations of these closures should be considered in future similar work [18]. In particular here the short connection length means that parallel temperature gradients are small, and the heat loss is primarily determined by the sheath.

The outer wall of the device is at $r = 10$cm, so that the distance between the last closed flux surface (LCFS) and wall is approximately 15mm ($16\rho_s$). This is challenging for modelling and is moreover is comparable to typical SOL widths at the outboard midplane leading to possibly strong interaction with the outer boundary in the numerical simulations. The poloidal cross-section of filamentary structures observed in the edge of tokamaks and similar devices are typically several ρ_s in size (e.g [19]) so we do not

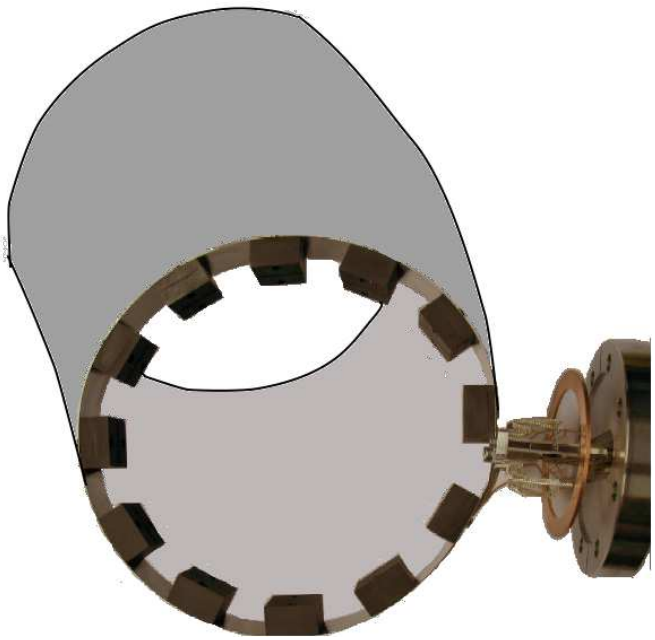

Figure 1. Toroidal section of the ISTTOK tokamak, showing the segmented poloidal limiter

expect many radial correlation lengths in the turbulence between the LCFS and wall. In section 3 we therefore analyse five radial locations, separated by 5mm ($\sim 5.5\rho_s$). This spacing is smaller than the radial correlation lengths of $10-15$mm reported in previous ISTTOK experimental studies [20].

ISTTOK is equipped with different Langmuir probe systems for the characterization of the edge plasma. A Langmuir probe system installed at a low-field-side (LFS) equatorial port, 75° toroidally from the limiter, is used to measure simultaneously the floating potential (V_f) and the ion saturation current (I_{sat}). Plasma parameters are measured in the scrape-off layer (SOL) and in the edge plasma (region just inside the last closed flux surface, LCFS) with the probe position varied from from pulse to pulse. Estimation of the probe area for collection of ion saturation current is complicated by ion-orbit effects, but is estimated as 6mm^2. In the analysis presented in this paper plasma parameters are typically obtained from a 5 ms time window during the discharge flat-top (≈ 15 ms).

The experimental data is acquired with a sampling frequency of 2MHz via a first order Butterworth filter at 250kHz, described by a transfer function given in equation 1.

$$H(f) = \left[1 + \left(\frac{f}{250\text{kHz}}\right)\right]^{-1} \tag{1}$$

Because the filter is not a sharp cut-off, significant experimental signal above noise levels is still seen experimentally to at least the 1MHz analysed here.

To enable comparison between experimental and simulation data, this filter is applied to the simulation output data by Fourier transforming the data, multiplying

by the above transfer function, and inverse transforming to obtain the filtered signal. This filtered signal is then subjected to the same analysis as the experimental data, with results given in section 3. Note that noise is not added to the simulation data; it has been found that this noise can make comparison to experimental skewness measurements challenging [21].

2.2. GBS

The GBS code [11, 10] is a 3D, five-field fluid code, based on the drift-reduced Braginskii equations [16]. Although not used in the present work, GBS is able to describe turbulence in diverted geometries [22], and it allows the self-consistent coupling of the plasma equations with a kinetic solver for the neutral particles [23]. GBS is able to evolve the plasma profiles in the plasma edge region, which includes both the SOL and the edge region, with no separation between equilibrium and fluctuating quantities. GBS has been used to simulate blob dynamics in TORPEX [8] and MAST [9], as well as plasma turbulence in TCV [24, 25], RFX-mod [26], Alcator C-Mod [27, 28], and ISTTOK [17]. With respect to the previous ISTTOK simulations [17], the simulations used for this work include both open and closed-field line regions, and evolve both the electron and ion temperature profiles. In the radial direction and at the limiter plates, Neumann boundary conditions are emplyed for density, temperature, electric potential, while Dirichlet boundary conditions are used for the vorticity.

2.3. Hermes/BOUT++

Hermes [12] is a 3D, five-field (cold-ion) model based on the Simakov-Catto drift-reduced equations [29], and solved using the BOUT++ framework [13, 30] in curvilinear coordinates. Hermes has been applied to turbulence in linear devices [31] including the interaction between plasma and neutral gas [32], limiter and diverted tokamaks [12]. For simulations of the poloidally-limited ISTTOK device, the geometry includes both open and closed field-line regions, and the coordinate system uses the poloidal plane as the drift plane (X-Z in BOUT++ coordinates). In the results shown here a resolution of 132 radial points (including 4 boundary cells) and 512 poloidal points. This corresponds to a radial resolution of approximately 0.15mm, and poloidal resolution of around 1mm. In the direction parallel to the magnetic field 16 points are used in a toroidal turn. The poloidal limiter is treated as continuous, as in the GBS simulations, and a Bohm sheath boundary condition is applied at the sheath entrance. In the radial direction zero-gradient (Neumann) boundary conditions are applied to all evolving fields (density, pressure, vorticity, electron and ion parallel velocities) on both inner and outer boundaries. For the electrostatic potential a Neumann boundary is used on the inner (core) boundary, and on the outer boundary ϕ is fixed to $2.8T_e$, the voltage which results in zero net sheath current.

The Hermes source code and ISTTOK input files are available at `https://github.com/boutproject/hermes`.

2.4. HESEL

HESEL, (Hot-Edge-Sol-Electrostatic) is an energy-conserving, 2D four-field Braginskii model governing the dynamics of a quasi-neutral, single species plasma [14]. It describes interchange-driven, low-frequency turbulence in a plane perpendicular to the magnetic field at the outboard midplane. For constant ion pressure the model reduces to the ESEL model, which has successfully modelled fluctuations and profiles in JET [33], MAST [34], EAST [35], and TCV [36]. Transition from the confined region to the region of open field lines is included in the model, through a change in the parallel closures, as well as the full development of the profiles across the LCFS. On closed field lines drift wave dynamics is included and on open field lines parallel losses from adiabatic expansion and sheath dissipation is included.

The effect of the parallel dynamics treatment was assessed in [17], where 2D and 3D GBS simulations were compared. The main impact of this simplification is to remove the drift wave in open field-line regions. This was found to have a significant impact on global profiles, with the High Field Side (HFS) being most affected. Transport at the LFS, where measurements are taken here, was less affected due to the strong ballooning drive.

In the radial direction on the inner (core) boundary the density, pressure and vorticity are fixed (Dirichlet conditions), and electrostatic potential has zero gradient (Neumann conditions). On the outer (wall) boundary a Neumann boundary is applied to density, pressure and vorticity, while the potential is fixed to $\phi = 0$ [37]. Note that due to low parallel connection length in ISTTOK, as discussed in section 2.1, parallel conduction for electrons is not active in this version of HESEL. The model assumption is therefore that electron temperature is constant along the magnetic field, so that heat losses in the SOL are set by the sheath heat transmission.

2.5. TOKAM3X

The TOKAM3X code is a 3D fluid code that is based on the moments of the Vlasov equation with Braginskii-like closures (similar to the other codes used here). The version of TOKAM3X used here solves four equations: the particle density continuity equation, the current conservation equation, the parallel momentum balance equation, and the parallel Ohm's law. The model is electrostatic, isothermal and uses adiabatic electrons for modelling edge plasmas in magnetically confined devices. The model, like the others used in this study, has been verified and compared to experimental cases [8, 9, 7] with encouraging results.

In this study the geometric flexibility of TOKAM3X was used to assess the impact of the segmented limiter, but in a laminar regime without drifts, and so without turbulent fluctuations. Turbulent statistics are therefore not shown for TOKAM3X in section 3, but a detailed comparison of limiter geometry effects is shown in section 4.1.

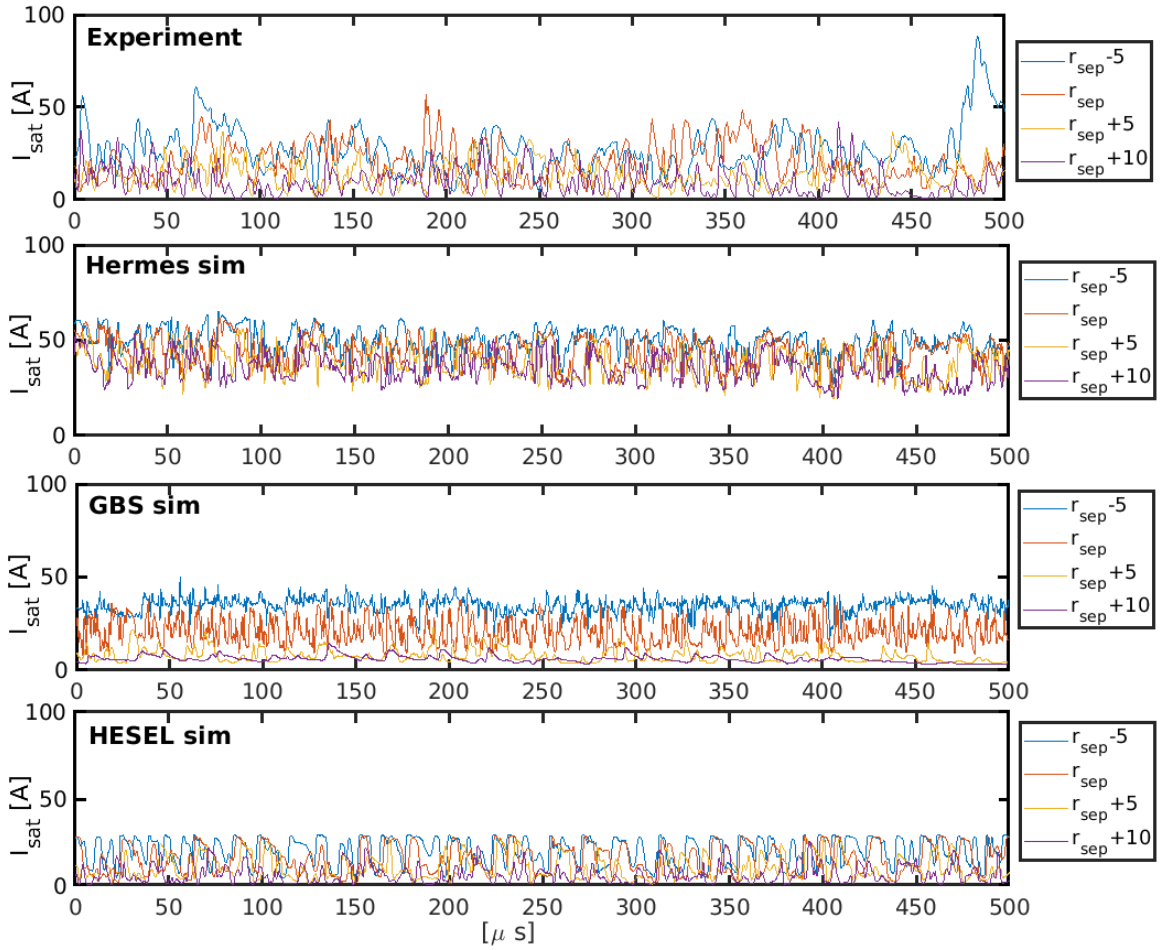

Figure 2. Time-series I_{sat} from various radial positions from experiment and simulations. The colour code represents the outermost four (of five) radial positions sampled.

3. Results

To compare outputs between experiment and simulation (figure 2), the data source is converted to SI units and then the analysis code is applied to all datasets, ensuring that any observed differences are due to the data and not due to the analysis process. The I_{sat} data sampled from the experiment and the simulations at the radial positions (taken with respect to the separatrix radial location) with a 5 mm radial separation are shown in figure 2. ‡.

Looking at the conditionally averaged shape of the "bursty" portions of the I_{sat} signal that exceeds the signal mean by at least two standard deviations, it is seen in figure 3 that such bursts are typically associated with filaments and are of the order of the timescale of this recovered bursty waveform. As seen, the average length of such

‡ Any low frequency fluctuations from the data if present were removed by a moving average method (over periods of 10 % the complete timeseries length > burst timescale) so as to only conserve the true signal bursts above the local mean.

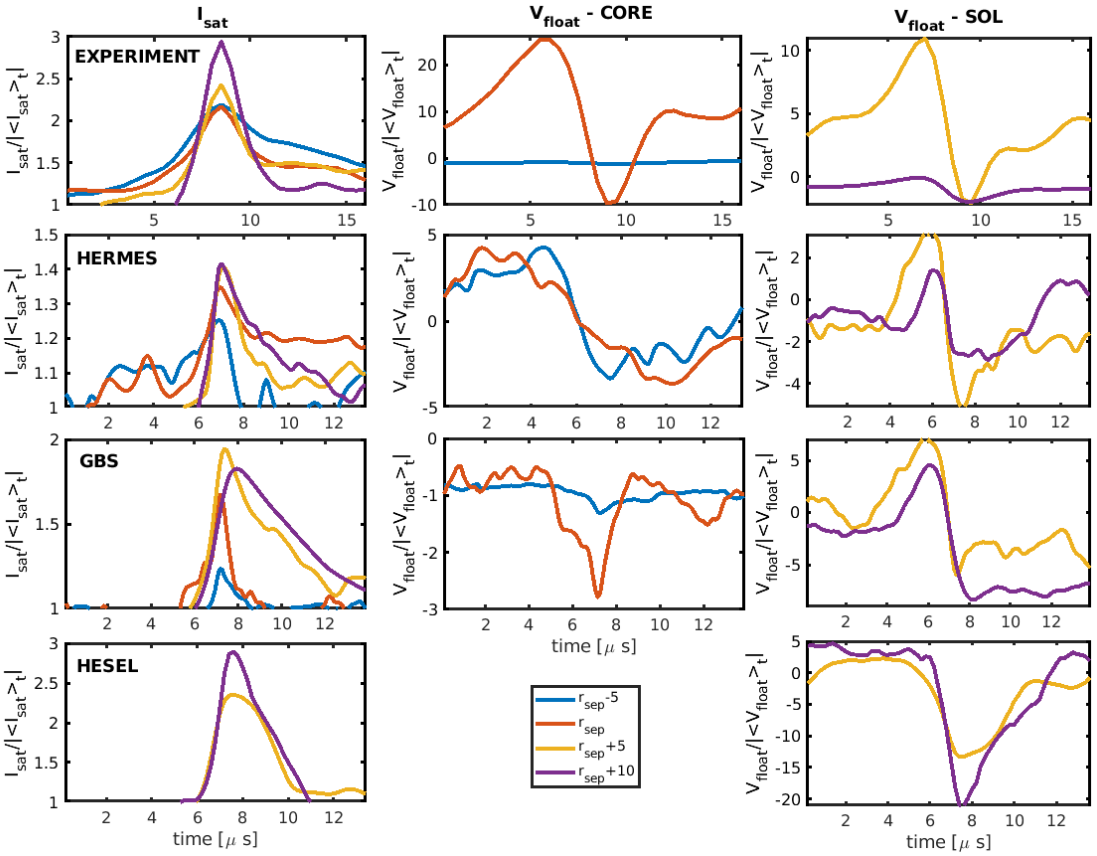

Figure 3. Conditionally averaged waveforms of the I_{sat} signal (left) and V_{float} signal from various radial positions from experiment and simulations, after being normalised by the absolute signal mean value. The colour code is for the radial positions sampled in each case, and the trigger used on the I_{sat} signal was 2 standard deviations from the mean. The first column corresponds to the I_{sat} signal while the second and third columns correspond the the V_{float} signal in the core and the SOL respectively. Data from radial locations that didn't fulfill the trigger conditions are absent for HESEL in the core.

signal bursts for the experiment is of the order of 10 μs and most of the simulations recover signal bursts of the same order at least for the radial positions in the SOL. While there continue to exist differences between experiment and simulations (and also within individual simulations models), the data for the radial positions beyond the separatrix (i.e. yellow and purple curves; at separatrix shown in red) show similarity in timescale of the average burst detected across all datasets with minor differences. This is also reaffirmed to some extent by looking at the associated average floating potential waveform for these bursts with a notable fall in the relative signal strength around same time: all codes recover comparable orders of magnitude in the SOL.

A Butterworth filter at 250kHz (equation 1) is applied to the simulation data, to mimic the filter used experimentally. This is done for all analysis described henceforward in this section (not just for the power spectral density), so that the impact on the distribution functions is also accounted for. The probe system is assumed to have a

single-point geometry, and any impact of the probe's geometry on plasma dynamics is not included in the simulations since total probe cross-section area was small compared to the SOL radial extent (probe C.S. area = 6 mm^2) and still larger than the electron Larmor radius in the SOL.

3.1. Mean profiles and fluctuation levels

Calculation of high order moments from turbulence statistics requires long timeseries data, due to the strong dependence on extreme events and the typically long-tailed distributions of fluctuations in tokamak edge plasmas [38]. Here estimates of the error in these statistical moments are calculated using the Bootstrap [39] method: a random sample of the same length as the original dataset is repeatedly drawn from the data, in this case 4000 times, so that some values are repeated and others omitted. The result is re-calculated using this random sample, and the 95% confidence interval is calculated from the resulting distribution of values. As a further test, we perform the analysis on half the timeseries, to check that the values have converged.

Ion saturation current I_{sat} are measured using a Langmuir probe as described in section 2.1. The mean I_{sat} radial profiles are qualitatively close in trend to the experimental trend with similar slopes, except for the Hermes data which are larger by a factor of 2. The ion sonic radius ρ_s is approximately 0.9mm, so that the ion-scale structures modelled by fluid turbulence codes here are expected to be of comparable size to the 15mm width of the SOL. Five radial locations are therefore chosen for analysis of the simulation outputs, at intervals of 5mm: Two points in the SOL, two inside the separatrix, and one at the separatrix.

To calculate the synthetic I_{sat} signal from simulation outputs, the effective area of the probe electrode needs to be taken into account. Analysis is complicated by the oblique angle of intersection of the probe electrode with the plasma, and finite ion orbit effects. Here we use an effective area to account for these effects. The calculation is the same for all simulations, but there may be a systematic error between the simulations and the experiment, due to this uncertainty. The I_{sat} signal is calculated as:

$$I_{sat} = 0.5 e A n_e \sqrt{\frac{eT_e}{m_i}} \tag{2}$$

where $A = 6\text{mm}^2$ is the area of the probe, n_e is the electron density, T_e the temperature (in eV), and m_i the ion mass (hydrogen). The resulting signal is then processed with a low-pass Butterworth filter to mimic the experimental diagnostic, as described in section 2.1. The filtered data is then analysed with the experimental data, and shown in figure 4. The mean profiles from HESEL and GBS simulations are close to experiment, within 30% at the separatrix, but Hermes values are around a factor of 2 too high, due to the plasma density being higher in these simulations.

The second diagnostic compared here is the floating potential V_{float}, which is calculated from the simulation outputs as $V_{float} = \phi - 3T_e$. The radial profiles of

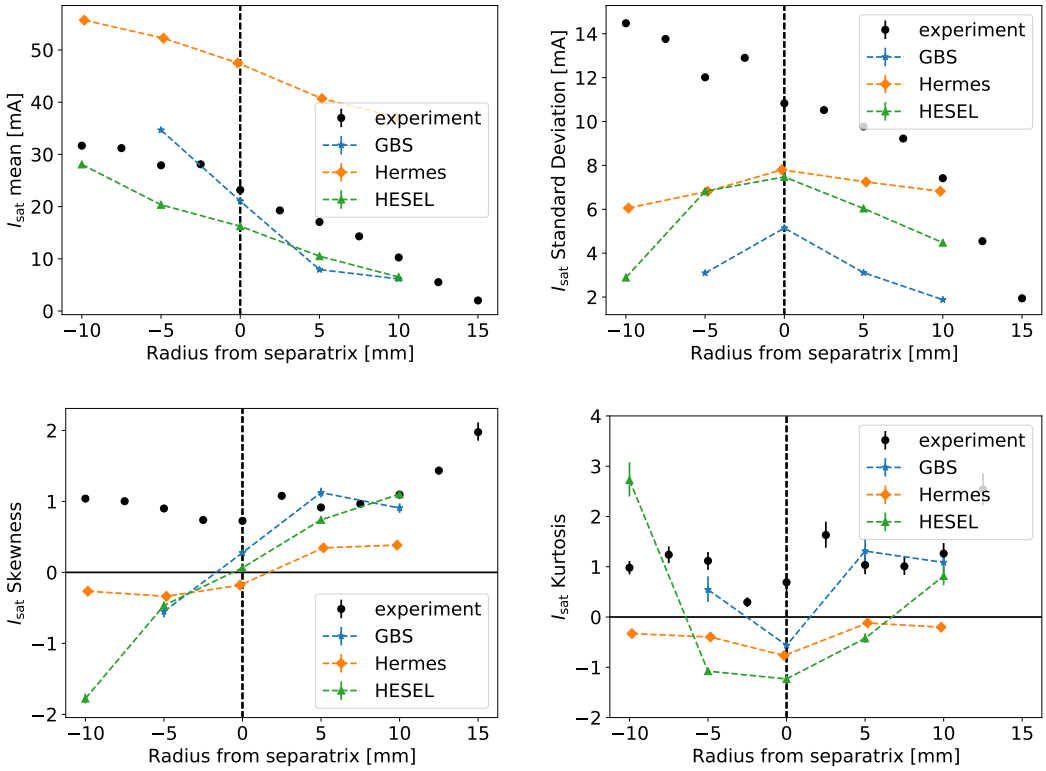

Figure 4. Statistical moments of the ion saturation current I_{sat}. Error bars are calculated using the bootstrap method as described in section 3.1. The vertical dashed line marks the separatrix.

statistical moments are shown in figure 5. There is a significant difference between the mean V_{float} profiles close to and just inside the separatrix when comparing the simulations to experiment, and also between simulations. These profiles are sensitive to poloidal rotation of the plasma via the $E \times B$ motion, i.e the radial electric potential gradient (see figure 6). This rotation impacts the turbulence, and is self-consistently determined by momentum transport processes including turbulence-generated Reynolds stress. In the simulations, potential gradients approach the experiment in trends and magnitude only inside the SOL, away from the separatrix for most cases. This is more clear in the I_{sat} gradient length for the portion immediately outside the separatrix (figure 6) which can be used as a proxy for density gradient length (assuming a linear T_e radial profile, it will translate into very similar trend for the density gradient length since it scales with $T_e^{-0.5}$ via equation 2), where the slopes of the profiles are comparable, despite the lack of sufficient radial points. The absence of full core in the simulations and sufficient radial points in the far SOL makes the near SOL immediately outside the separatrix as the most appropriate region for drawing comparisons between simulation and experiment, as well as comparing simulations amongst themselves.

The experimental profiles may also be affected by mechanisms and external momentum sources [40] not present in these simulations, making it challenging to

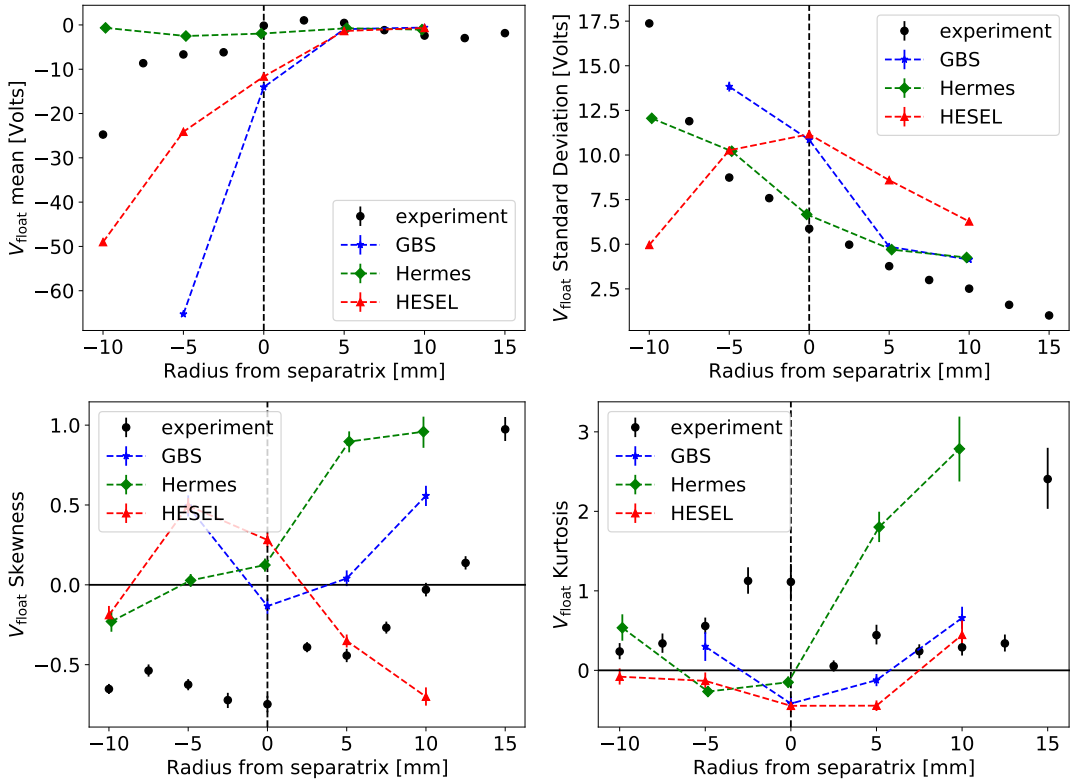

Figure 5. Statistical moments of the floating potential. Error bars are calculated using the bootstrap method as described in section 3.1. The vertical dashed line marks the separatrix.

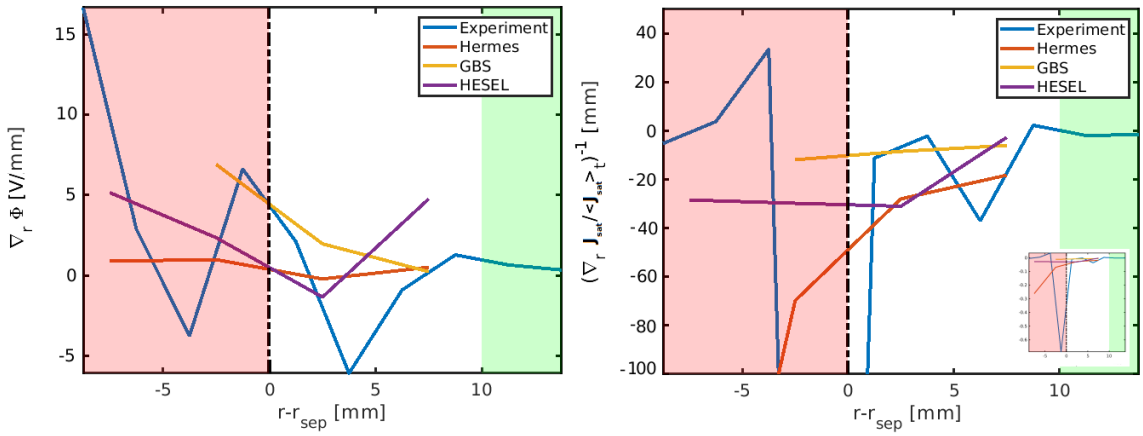

Figure 6. Average floating potential radial gradient (left), and average I_{sat} radial gradient length (with the full profile inset in the right-bottom) - the scale for the experimental curve is not comparable to the simulations in the core but becomes comparable only in the near-SOL.

compare with the experiment. Further, unlike other evolved fields in the simulations, the electrostatic potential is calculated by inverting an elliptic operator in all these drift-reduced models. This makes the solution sensitive to the choice of boundary conditions. In the codes used here the boundary conditions employed for the electrostatic potential ϕ are Neumann (zero-gradient) at the core, and Dirichlet (fixed value) at the outer wall boundary. Physically this corresponds to setting the radial electric field at the inner boundary to zero i.e. zero mean poloidal flow at the inner boundary, and no restriction on the poloidal flow on the outer boundary. Improving understanding of the plasma flow evolution is crucial to a proper validation of the simulation codes, but is beyond the scope of this study (since generating flows self-consistently is not possible without modeling the core completely [41]). Further progress will require dedicated experiments and measurement of the plasma potential, for example using ball pen probes [42, 43], which have been used in ISTTOK experiments [42] but were not available for this study.

3.2. Probability density functions

Having discussed the differences in the low moments (mean and standard deviation) between experiment and simulation data, we now focus on differences in the shape of the distribution functions and the Fourier power spectra. This provides additional insight because in principle many different distribution functions can generate the same moments. The distribution functions for I_{sat} fluctuations are compared in figure 7, normalising each signal to a mean of zero and standard deviation of 1.

Several interesting features can be seen in figure 7: Outside the separatrix all codes are able to reproduce the experimentally observed long tail of positive fluctuations. This is in agreement with previous experimental and theoretical observations that the dynamics in the scrape-off layer of magnetised devices is quite universal [44, 45]. As a result, it is not a good discriminator between models, provided they have the required basic ingredients of interchange curvature drive and parallel loss. An interesting difference between distributions in the SOL at $r = 10$mm is that both GBS and Hermes have longer negative tails than HESEL or the experiment. A possible reason may be due to differences in the parallel transport models, which are similar between 3D codes GBS and Hermes, and different for HESEL; this could affect the background through which the filaments propagate. Further studies of mean profiles would be needed to resolve this in any future follow-up work.

At the separatrix (and even beyond), the overall shape of the distribution function is well reproduced showing the concurrence between codes with experiment on the shape of the distribution function of I_{sat} fluctuations. There is a feature at around $+1.5\sigma$ in the HESEL results inside the separatrix, which is thought to be an artifact of the way in which profiles are maintained in the core (by forcing the profiles towards specified values). This is not present in other codes, which are purely flux driven.

To put these comparisons in perspective, the two-sided Kolmogorov-Smirnov test [46, 39] is used to test the null hypothesis that the simulated fluctuations are drawn

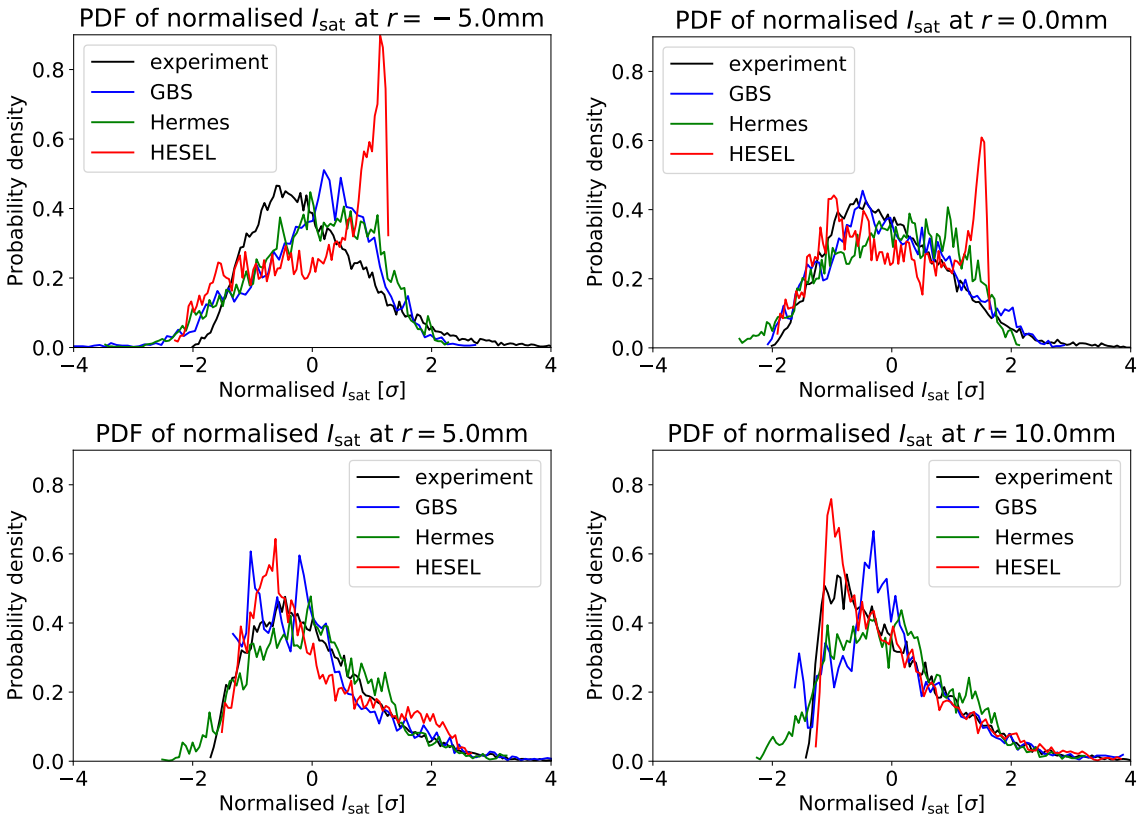

Figure 7. Normalised Probability Density Functions for I_{sat} fluctuations at radial locations across the separatrix. Each signal has a mean of zero and standard deviation of one, to remove differences due to calculation of I_{sat} from density and temperature.

from experimental datasets having the same distribution. This method calculates the supremum of the difference between the cumulative probability distribution functions of two sets of independent and identically distributed values, labelled "Max CDF difference" in table 1. This difference is then used to calculate a probability that the null hypothesis is consistent with the observations. The lower the p-values the more significant the difference between the distribution of the (simulation) data from the reference (experimental) distribution. We use the implementation of this algorithm from SciPy (`scipy.stats.ks_2samp`)[47].

The absolute difference between the simulation and experimental distributions, shown in table 1, is relatively small, less than 0.09 when all samples are used, but the large number of samples means that the p-values are all smaller than 10^{-3}, indicating a significant difference between the distributions. This conclusion is however sensitive to the rate of sampling: The assumption of independent samples in the Kolmogorov-Smirnov statistic is not justified here, since the signals contain multiple data points as a plasma filament or structure crosses the probe. This can be seen in figure 3, where the scale of the horizontal axis is of the order of 10μs. Time intervals much shorter than this are likely to be affected by auto-correlation in the signals.

The interval between samples vary between experiments and simulations, so in

Table 1. Kolmogorov-Smirnov statistic for normalised I_{sat} distribution functions shown in figure 7. The maximum difference between the Cumulative Distribution Function (CDF) calculated from the experimental and simulation data, along with the probability (p-value) that this is consistent with both samples being drawn from the same distribution. Sampling intervals from experiment are 5μs; GBS 0.111μs; Hermes 0.104μs; HESEL 0.209μs.

	Max CDF difference			p-value		
$r - r_{sep}$	GBS	Hermes	HESEL	GBS	Hermes	HESEL
Every sample						
0 mm	0.05	0.07	0.08	0.00	0.00	0.00
5 mm	0.04	0.09	0.02	0.00	0.00	0.01
10 mm	0.08	0.07	0.06	0.00	0.00	0.00
Sampling at 10μs intervals						
0 mm	0.09	0.10	0.11	0.61	0.27	0.09
5 mm	0.08	0.12	0.08	0.79	0.08	0.43
10 mm	0.11	0.08	0.08	0.43	0.48	0.42
Sampling at 50μs intervals						
0 mm	0.16	0.19	0.18	0.86	0.42	0.37
5 mm	0.31	0.20	0.09	0.16	0.32	0.99
10 mm	0.19	0.18	0.12	0.70	0.45	0.86

table 1 comparisons are also made between datasets which have been sub-sampled to 10μs and 50μs (rounding to the nearest integer sample), to reduce the correlation between samples. At these sampling rates the difference between distributions are likely not statistically significant (p-values to values above 0.05); it is possible that longer timeseries would result in smaller p-values (more significant difference). Note that the relative values of p between simulation codes (GBS, Hermes, HESEL) are not indicative of better or worse matches to experiment, and in this case all simulation results are statistically similar. From this analysis we conclude that the quantitative differences given in table 1 are a useful measure of differences in statistical distribution, but that the p-values are too sensitive to auto-correlation in the signals to be reliable.

Following the analysis of the I_{sat} signals, we now compare the probability density functions for the normalised floating potential V_{float}, shown in figure 8. A visual comparison of the PDFs confirms the impression given by the moments in figure 5: simulation outputs have a wider spread (larger standard deviation) as compared to the experiment, with more positive excursions in the outer SOL and negative excursions at the separatrix. The experimental data close to the separatrix are also clearly skewed with a longer tail for negative values, as is typically observed[19]. The V_{float} PDF in the near SOL (r = 5mm) by Hermes is slightly positively skewed while that of HESEL is slightly negatively skewed (also seen earlier in figure). Farther out in the SOL (r = 10 mm), HESEL seems is theonly one to remain slightly positively skewed, while Hermes and GBS recover largely symmetric (but more pointed) PDFs. While models differ in

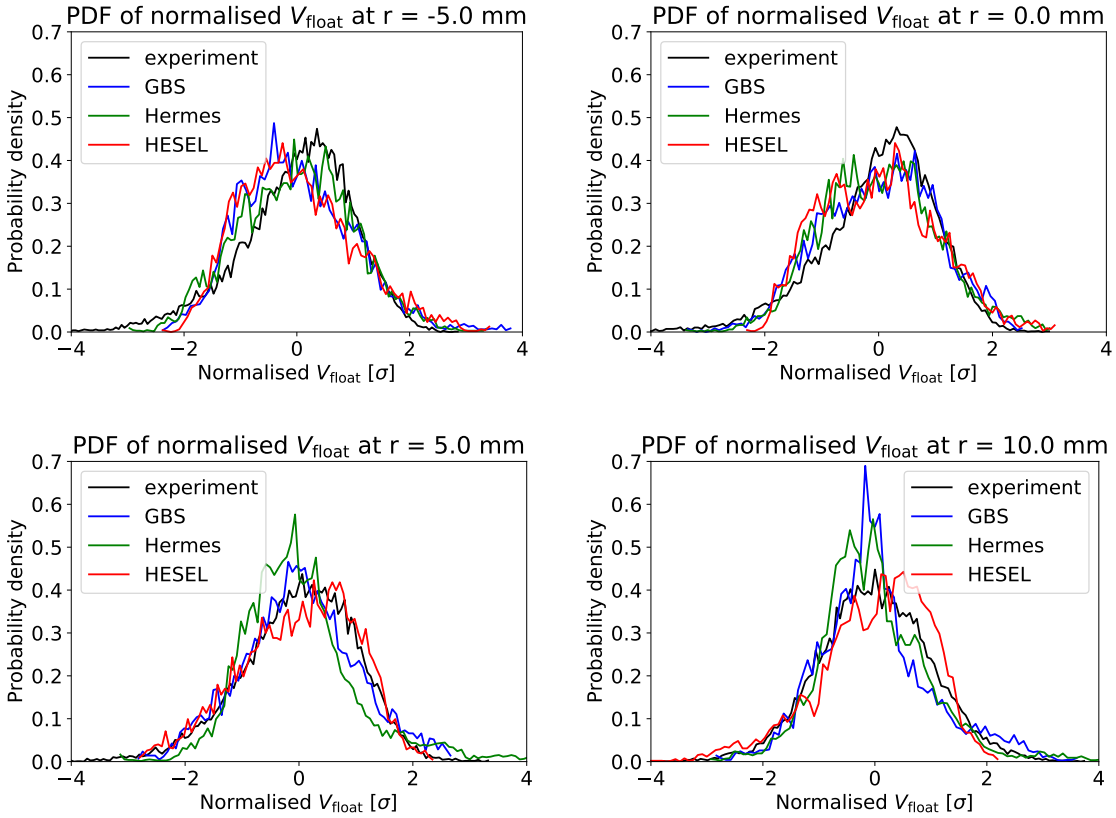

Figure 8. Probability Density Functions for V_{float} fluctuations, taken at the separatrix and two points in the SOL. Each PDF is normalised to a mean of zero and standard deviation of one, so that the distribution function shape can be more easily compared.

their formulation and implementations, they still remain comparable to the experiment. The simulated PDFs for the core region while comparable with experiment lack the rest of the core region which is the drive for the observed transport statistics in the core region for the experiment. And even if the core region statistics are overlooked, a visual comparison of the normalised PDFs in the SOL shows quite reasonable agreement with experiment.

The Kolmogorov-Smirnov test [46] applied to the normalised V_{float} data is shown in table 2. This analysis is of the normalised signals, which all have a mean of zero and standard deviation of 1. The sometimes large differences in these low moments shown in figure 5 are therefore not included; the measurement here is of the deviation between PDFs after these differences are accounted for. If all samples are included, the maximum difference between cumulative distribution functions is relatively small (less than 0.08 in all cases); The large number of samples means that this difference results in a small p-value (likelihood of both sets of data being drawn from the same distribution). As discussed above these values are likely to be affected by auto-correlation in the signals. Once the interval between samples is increased to a value comparable to (10μs) or larger than (50μs) the typical fluctuation timescale shown figure 3, the p-values increase such

Table 2. Kolmogorov-Smirnov statistic for the normalised V_{float} distribution functions shown in figure 8. The maximum difference between the Cumulative Distribution Function (CDF) calculated from the experimental and simulation data, along with the probability (p-value) that this is consistent with both samples being drawn from the same distribution. Sampling intervals from experiment are 5μs; GBS 0.111μs; Hermes 0.104μs; HESEL 0.209μs.

	Max CDF difference			p-value		
$r - r_{sep}$	GBS	Hermes	HESEL	GBS	Hermes	HESEL
Every sample						
0 mm	0.048	0.070	0.079	0.00	0.00	0.00
5 mm	0.038	0.091	0.024	0.00	0.00	0.007
10 mm	0.080	0.069	0.055	0.00	0.00	0.00
Sampling at 10μs intervals						
0 mm	0.095	0.098	0.11	0.61	0.27	0.086
5 mm	0.081	0.125	0.078	0.79	0.077	0.44
10 mm	0.11	0.082	0.079	0.43	0.48	0.42
Sampling at 50μs intervals						
0 mm	0.16	0.19	0.18	0.86	0.42	0.37
5 mm	0.31	0.20	0.09	0.16	0.32	0.99
10 mm	0.19	0.18	0.12	0.70	0.46	0.86

that the difference is not significant at the 1σ level. This does not mean that there is no difference between simulation and experiment; the smaller number of samples reduces the significance, so that longer signals would be needed to distinguish between the PDFs. Our conclusion from visual inspection and Kolmogorov-Smirnov analysis of the I_{sat} and V_{float} PDFs is that in all cases the shapes of the distribution functions are statistically similar with the signal lengths used here (at least 1ms), once the differences in mean and standard deviation are removed.

3.3. Power spectral density

The power spectral density (PSD) for the normalised I_{sat} signals (all with mean of zero, standard deviation of 1) are shown in figure 9 for four of the outermost radial locations of the total five positions with respect to the separatrix. The same is presented for the raw V_{float} signals is in figure 10, and in both figures these are compared with the power spectral density of the corresponding experimental data.

In the ion saturation current (figure 9) there is substantial variation between the code results, but a common pattern is that more power is seen at low frequencies in the experimental data than in simulation results. At these low frequencies around 20kHz the filtering is negligible. This difference diminishes as one looks at data further outside radially. This is a good sign on the one hand, because the plasma dynamics inside the separatrix are largely influenced by boundary conditions used in each model (as

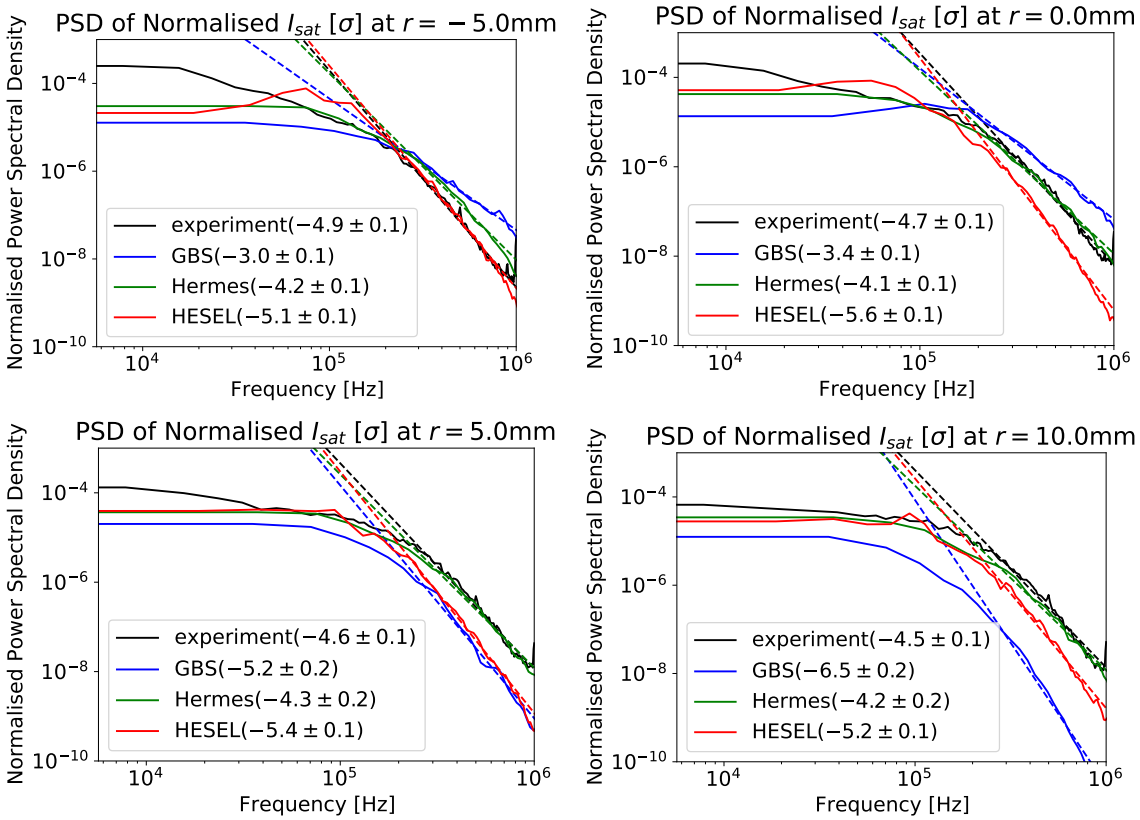

Figure 9. Power Spectral Density for normalised I_{sat} fluctuations. Each signal has a mean of zero and standard deviation of one, to remove differences due to calculation of I_{sat} from density and temperature. The frequency is truncated at 1MHz, the Nyquist frequency of the experimental data, which has a sample interval of 0.5μs. Dashed trend lines are fitted using linear least squares to the frequency range $200 - 800$kHz, with the gradient given in parentheses in the legend.

mentioned earlier). On the other hand, even after the PSD plot for the innermost radial position (r $= -5.0$mm) is ignored, the remaining trends recovered still differ in the high-frequency regime (with Hermes data best approaching experimental data) with some improvement as we move radially outward. Another common characteristic that is recovered by the three simulations is the frequency at which the slope changes, seen to be around $\simeq 200$kHz, which again seems to concur with the experimental data also. Above 200kHz the slopes of the power spectra have been fit using linear least-squares. Slopes from simulation data are scattered above and below the experimental value, but it is interesting to note that in most sources (experiment, Hermes and HESEL) the slope does not vary much with radius (e.g slopes from experimental data going outwards from $r = -5$mm to $r = 10$mm are -4.9 $\pm$ 0.1, -4.7 ± 0.1, -4.7 ± 0.1 and -4.5 ± 0.1) whereas GBS results show a steepening of the PSD slope with increasing radius from -3.0 ± 0.1 to -6.5 ± 0.2. This may reflect differences in high frequency dissipation mechanisms between closed and open field-line regions.

The floating potential PSD shown in figure 10 reveal a similar situation, with

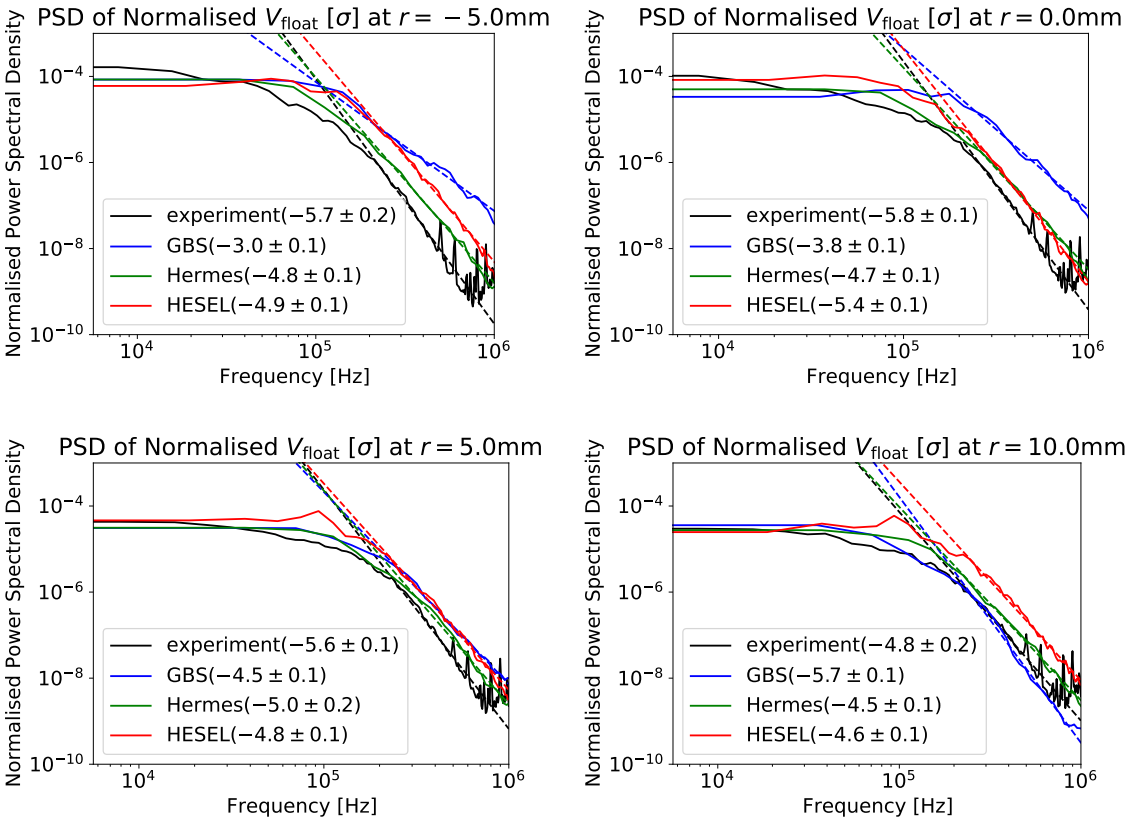

Figure 10. Power Spectral Density for normalised V_{float} fluctuations. The frequency is truncated at 1MHz, the Nyquist frequency of the experimental data, which has a sample interval of 0.5μs. Dashed trend lines are fitted using linear least squares to the frequency range $200 - 800$kHz, with the gradient given in parentheses in the legend.

improvements in trends generally noticeable as we move radially outward. Whereas the normalised I_{sat} simulation results generally have comparable or lower power in the high frequencies ($>$ 100kHz) than experimental data, normalised V_{float} simulation results have consistently higher power in the high frequencies than in experimental data. In the V_{float} PSD results there is noticeably higher noise in the experimental data in the high frequency range (roughly beyond 500kHz), as one nears the experimental sampling Nyquist frequency limit of 1MHz, which was not present in the I_{sat} data. This motivated the choice to fit slopes to frequencies below 800kHz, and the same range was applied to the I_{sat} data (figure 9).

The differences in high frequency characteristics is clearly seen in the slopes, which were fit to power spectral density between 200kHz and 800kHz: In almost all cases the experimental data has a steeper slope (lower relative power at high frequencies) than the simulated data; the exception is GBS data at $r = 10$mm. There are at least two potential explanations for this: The results in figure 10 may suggest that Langmuir probes are under-estimating the fluctuation levels at high frequencies, or that the filtering applied to the simulation data (equation 1) doesn't fully capture the

diagnostic response. Alternatively it may be that a damping mechanism present in experiment (for example plasma-neutral interactions) is not properly represented in the fluid turbulence models as used here.

4. Impact of the boundaries

A limitation of the analyses and statistics presented in the previous section was that the simulation data was not sampled at the same frequency as in the experiment - Hermes and GBS had a sample interval of about 0.1μs while for HESEL it was 0.2μs. Needless to say, statistical deviations in the high frequency range can be attributed to this difference even though attempts have been made to minimise its impact in the analyses here. A further aspect that could improve the quality of results would be to extract data for more radial positions in the simulations as in the experiment. While these issues can be rectified in future investigations, another important difference between experiment and simulations that needs to be considered while interpreting the results are the boundary conditions used in the simulations at the limiter target.

Since tokamak plasmas interact through electromagnetic fields involving different spatial and temporal scales, boundary conditions imposed can have a significant impact on the results. Ignoring atomic effects in the edge region, the modelling of edge plasmas in the fluid regime typically involves solving a fluid-reduced set of equations for fluid continuity, fluid momentum, Ohm's law, and temperature evolution under judiciously chosen approximations for the scales being solved within the restrictions of boundary effects imposed on the model. The calculation of the electric potential (and electromagnetic potential) in all the models used here involves the inversion of an elliptic equation for vorticity. The boundary conditions imposed on currents and electromagnetic fields in the SOL have an impact on the values away from the boundaries, as sampled in the experiment and simulations.

The Hermes/BOUT++ results were found to be sensitive to the core boundary conditions, in particular those which affected the radial electric field, responsible for poloidal E $\times$ B motion. Although the core region of the simulations was not the focus of the effort, the poloidal flows arising out of this region eventually influence the radial density gradient established at the separatrix which is in turn responsible for the interchange type instabilities (affecting filamentation or "bursty" fluctuations) farther outside. Developing consistent core boundary conditions for edge fluid codes while challenging is desirable for future more complex regimes of validation between experiment and simulation. In this work the importance of the issue is highlighted so that it may be addressed in future work, where one approach may be to simulate the whole device with accurate target geometry (e.g. [48]), and eventually including the core.

The impact of boundary conditions was most visible in the HESEL results which differed from GBS and HERMES results, especially in the inner core region. Furthermore, the approximations typically made in 2D models to compute the mean

fields (as compared to in 3D models) average out the parallel direction effects making it difficult to directly compare results between the two classes of codes. The mean statistics in all models however do closely resemble each other on a qualitative level. Besides the individual numerical treatment of boundary conditions across models, the type of target geometry approximated by each model is also important - for e.g., the use of a uniform poloidal limiter as against a discrete one (as is the case in the experiment). The limiter used in the ISTTOK experiment was poloidally segmented, but was modelled as poloidally continuous in the GBS, BOUT++ and HESEL simulations. Modelling it as discrete is discussed in more detail in the next subsection.

4.1. Continuous versus discrete limiter geometry

To study the general impact of the limiter geometry on the plasma properties, another code, TOKAM3X, was used which affords more versatile domain geometries and was described in section 2.5.

The limiter geometry used by the other codes was a poloidal limiter that extends over a poloidal angle $\theta = 0°$ to $360°$, whereas the real limiter in the ISTTOK experiment was segmented consisting of a series of 12 discrete equally sized poloidal blocks, equally spaced in the poloidal direction (fig. 1). While the inter-block poloidal distance is constant for all blocks, the distance is largest at the absolute edge of the wall where the blocks are affixed onto the wall, and reduces as one approaches the separatrix radially - this is due to the rectangular shape of the blocks with the same dimensions at the outside where it joins the wall, and inside at the separatrix. The impact of such a limiter geometry is to create magnetic field lines in the SOL that do not all have the same connection lengths as one moves from separatrix to the wall. Since about 68% of the periphery at the LCFS is covered by the target surface as against about 56% at the walls, this creates small regions of field lines that are longer near the separatrix (where the interblock distance is smaller), and large regions of such field lines near the walls (where the interblock distance is relatively larger).

The connection length of the SOL field lines is $L_\parallel \sim 2\pi R$ in the simulations with the continuous poloidal limiter. But in the experiment many of the field lines extend around the torus twice the $L_\parallel$ through the gaps between the limiter blocks before terminating on the limiter surface. This variation in connection length between the discrete and continuous limiter cases makes them non-equivalent, and this is seen to some extent in the laminar simulations performed using TOKAM3X. Another, although equivalent, way of interpreting the difference between the continuous and discrete limiter cases is via the total "wetted area"; in the case of the continuous limiter is about 2 times the wetted area of the discrete limiter case. So while the distance along which SOL-particles have to move before striking the targets is about twice as long, the area on which these particles arrive to is halved. This disparity between the the experiment and simulation SOL is what is highlighted in the analysis here.

To be able to study the impact of this, simulations are performed using the two

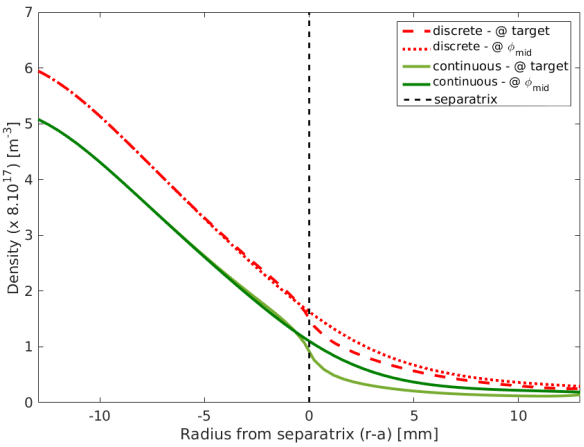

Figure 11. Radial density profiles averaged over poloidal angle, for a toroidal angle halfway between the two target surfaces.

limiter configurations - a continuous poloidal limiter as used by codes in the previous sections, and the realistic discrete poloidal block limiter (however, the inter-block distance is maintained constant for all radial positions in the simulations for the discrete poloidal limiter as though the blocks were designed to have a shorter length on the inside at the separatrix and longer length at the wall where they are affixed). This was done in a laminar plasma regime with no drifts so as to be able to study the impact of the limiters on a non-turbulent passive plasma as a first order approximation of the limiter geometry's role on the plasma. To do this, the perpendicular drifts were switched off. In doing so, we get an indication of a biased geometric "imprint" of the limiter on the plasma in the absence of any strong cross-field mixing of the plasma.

As could be expected, the simulations performed with TOKAM3X have shown that the average density in the simulation reaches a slightly higher mean value for the discrete limiter case (see radial density profiles in fig. 11) as compared to the continuous limiter case. In fig. 4.1 (right), the presence of the discrete block limiter is clearly visible by the presence of the 12 patches regularly arranged in the poloidal direction in the SOL at the toroidal angle where the limiter is placed. For example, In fig. 4.1 (top, left), the continuous poloidal limiter's presence is indicated by the continuous near-zero low density region in the poloidal direction in the SOL. The shadow of these limiters is visible even farther away from their vicinity inside the SOL, as seen in the fig. 4.1 (bottom). The density map patches are however less pronounced here owing to some cross-field mixing due to perpendicular diffusion.

The discrete limiter configuration leaves a clear imprint of its presence in the plasma. This becomes more obvious when looking at the poloidal profile of the density in the SOL as shown in fig. 13. Here we see the clear difference between the discrete and continuous cases even for a toroidal angle that is much removed from the target loca-

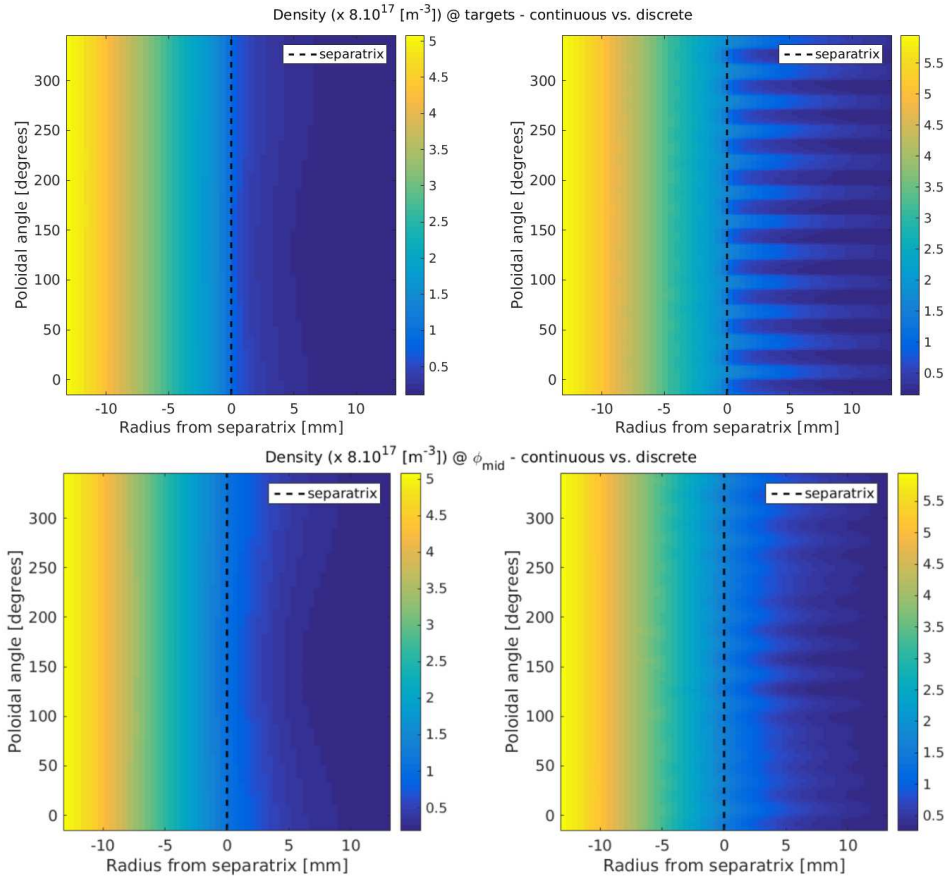

Figure 12. Density colour maps of the poloidal cross-section: (top row) at the target location , and (bottom row) for a toroidal angle halfway between the two target surfaces, for the continuous limiter (left) and discrete block limiter (right). The poloidal plane is represented in Cartesian coordinates.

tion. On careful observation of the discrete limiter curves (red colour), it is seen that for poloidal angle $\theta \sim 50°$ - $225°$, the peaks in the profile at the target coincide with the troughs in the profile away from the target, suggesting a role of the inequality of field line lengths in this region between the two cases. But to get a better picture of this magnetic shearing in the SOL, further studies would be needed to be carried out by varying q. But if it is only for the sake of identifying the presence of any strong bias present due to limiter geometry, from the above analysis it is clear that the limiter geometry does indeed influence plasma density profiles far away from the limiter. To this, the addition of drifts and turbulent transport that lead to more mixing via cross-field transport, would eventually reveal the full extent of the limiter geometry's impact on transport. This might explain some of the differences seen earlier between results of simulations and experiment especially in mean field values and fluctuation standard deviations.

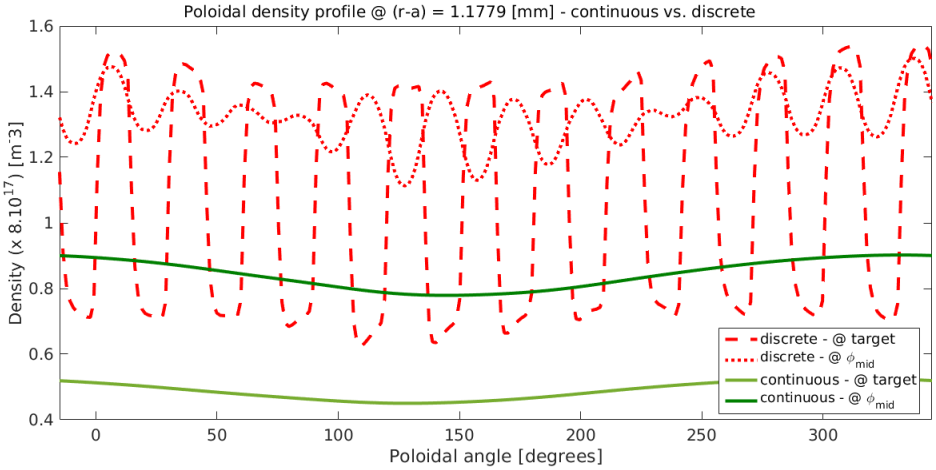

Figure 13. Time-averaged poloidal density profiles for a given radial position $r - a \simeq 1.18mm$

5. Conclusions

The main statistical results from all numerical models have reproduced the mean plasma experimental behaviour with varying degrees of fidelity, based on individual code strengths and limitations. While near-SOL behaviour is challenging to reproduce with the absence of a truly self-consistent core that includes all external momentum effects present in the experiment, the models have shown that beyond the separatrix there is a good degree of agreement in terms of the mean fluctuations statistics recovered. Nonparametric statistical methods such as the Bootstrap method (used to calculate errors on high order moments) and Kolmogorov-Smirnov tests (used to compare PDFs) are useful tools, but care should be taken in their interpretation. Usually long turbulent timeseries are required if conclusions are to be drawn from statistically significant results.

The differences between models become more evident while looking at detailed statistical features like PDFs and power spectra, while also bringing out the limitations of such comparisons with data that is not all sampled in the same manner. This is a key point to be noted for any further validation exercise between codes while designing and conducting such validation exercises. The convergence of all three models in many of the aspects also demonstrates the inter-comparability between different numerical model data when their underlying approximations and hypotheses are known.

Neutral dynamics and impact on turbulence has been found in some studies to have a modest impact on turbulence characteristics [49]. The simulations here do not include neutrals, though the codes used can include neutral gas models. Future studies could incorporate these effects, to better approximate experimental conditions.

The challenge remains in reconciling the boundary conditions as these are individual characteristic features of each model, in some cases lending more detail to the model's ability to simulate the physics of interest like in the case of HESEL. Indeed here the 2D HESEL simulations, performed at the LFS, are found to reproduce many aspects of

the experimental data, in spite of not including target geometry information. The 3D models seemed to qualitatively approach aspects of experimental data, like in the case of PDFs and PSDs recovered for the I_{sat}.

Apart from the absence of many physical effects from the fluid models, in the last section we demonstrated the presence of a bias present in the simulated data by the choice to approximate the target geometry as a continuous poloidal limiter instead of a discrete one. This bias ensured the absence of more realistic effects of the target geometry on simulated data. This affected upstream mean values, thereby showing how important an effect certain approximations and assumptions used in modelling edge plasmas can have on the results recovered from such models.

The experimental data, simulation outputs, and analysis scripts used in this publication are available on Zenodo, DOI `https://doi.org/10.5281/zenodo.4043994`.

Acknowledgments

This work has been carried out within the framework of the EUROfusion Consortium and has received funding from the Euratom research and training programme 2014–2018 and 2019–2020 under grant agreement No 633053. The views and opinions expressed herein do not necessarily reflect those of the European Commission.

References

[1] P C Stangeby. *The Plasma Boundary of Magnetic Fusion Devices*. IoP, 2000.

[2] ITER Physics Expert Group on Divertor. Progress in the ITER physics basis, chapter 4: Power and particle control. *Nucl. Fusion*, 39:2391, 1999.

[3] T Eich et al. Scaling of the tokamak near the scrape-off layer H-mode power width and implications for ITER. *Nucl. Fusion*, 53:093031, 2013.

[4] R J Goldston. Heuristic drift-based model of the power scrape-off width in low-gas-puff H-mode tokamaks. *Nucl. Fusion*, 52:013009, 2012.

[5] F Riva, P Ricci, F D Halpern, S Jolliet, J Loizu, and A Mosetto. *Physics of Plasmas*, 21:062301, 2014.

[6] B D Dudson, J Madsen, J Omotani, P Hill, L Easy, and M Loiten. *Physics of Plasmas*, 23(6):062303, 2015.

[7] P Tamain, H Bufferand, G Ciraolo, C Colin, D Galassi, Ph. Ghendrih, F Schwander, and E Serre. *J. Comput. Phys.*, 321:606–623, 2016.

[8] F Riva, C Colin, J Denis, L Easy, I Furno, J Madsen, F Militello, V Naulin, A H Nielsen, J M B Olsen, J T Omotani, J J Rasmussen, P Ricci, E Serre, P Tamain, and C Theiler. Blob dynamics in the torpex experiment: a multi-code validation. *Plasma Physics and Controlled Fusion*, 58(4):044005, 2016.

[9] F Militello, N R Walkden, T Farley, W A Gracias, J Olsen, F Riva, L Easy, N Fedorczak, I Lupelli, J Madsen, A H Nielsen, P Ricci, P Tamain, and J Young. Multi-code analysis of scrape-off layer filament dynamics in mast. *Plasma Physics and Controlled Fusion*, 58(10):105002, 2016.

[10] F. D. Halpern, P. Ricci, S. Jolliet, J. Loizu, J. Morales, A. Mosetto, F. Musil, F. Riva, T. M. Tran, and C. Wersal. The GBS code for tokamak scrape-off layer simulations. *Journal of Computational Physics*, 315:388–408, June 2016.

[11] P Ricci, F D Halpern, S Jolliet, J Loizu, A Mosetto, A Fasoli, I Furno, and C Theiler. *Plasma Phys. Control. Fusion*, 54:124047, 2012.
[12] B D Dudson and J Leddy. *Plasma Phys. Control. Fusion*, 59:054010, 2017.
[13] B D Dudson et al. *Comp. Phys. Comm.*, 180:1467–1480, 2009.
[14] J. Madsen, V. Naulin, A. H. Nielsen, and J. Juul Rasmussen. Collisional transport across the magnetic field in drift-fluid models. *Physics of Plasmas*, 23(3):032306, 2016.
[15] P Tamain, Ph Ghendrih, E Tsitrone, V Grandgirard, X Garbet, Y Sarazin, E Serre, G Ciraolo, and G Chiavassa. *J. Comput. Phys.*, 229(2):361–378, 2010.
[16] A. Zeiler, J.F. Drake, and B. Rogers. Nonlinear reduced Braginskii equations with ion thermal dynamics in toroidal plasma. *Phys. Plasmas*, 4(1997):2134, 1997.
[17] R Jorge, P Ricci, F D Halpern, N F Loureiro, and C Silva. *Physics of Plasmas*, 23:102511, 2016.
[18] J P Brodrick et al. Testing nonlocal models of electron thermal conduction for magnetic and inertial confinement fusion applications. *Physics of Plasmas*, 24:092309, 2017.
[19] D A D'Ippolito, J R Myra, and S J Zweben. *Physics of Plasmas*, 18:060501, 2011.
[20] B Liu, C Silva, H Figueiredo, M A Pedrosa, B.Ph van Milligen, T Pereira, U Losada, and C Hidalgo. Multi-scale study of the isotope effect in isttok. *Nuclear Fusion*, page 056012, 2016.
[21] A H Nielsen et al. *Nucl. Fusion*, 59:086059, 2019.
[22] P Paruta, P Ricci, F Riva, C Wersal, C Beadle, and B Frei. Simulation of plasma turbulence in the periphery of diverted tokamak by using the GBS code. *Physics of Plasmas*, 25:112301, 2018.
[23] C. Wersal and P. Ricci. Impact of neutral density fluctuations on gas puff imaging diagnostics. *Nuclear Fusion*, 57(11):116018, 2017.
[24] F. Nespoli, I. Furno, F.D. Halpern, B. Labit, J. Loizu, P. Ricci, and F. Riva. Non-linear simulations of the TCV scrape-off layer. *Nuclear Materials and Energy*, 12(Supplement C):1205 – 1208, 2017. Proceedings of the 22nd International Conference on Plasma Surface Interactions 2016, 22nd PSI.
[25] F Riva et al. Shaping effects on scrape-off layer plasma turbulence: A rigorous validation of three-dimensional simulations against TCV measurements. *Physics of Plasmas*, 27:012301, 2020.
[26] F Riva et al. Three-dimensional simulations of plasma turbulence in the RFX-mod scrape-off layer and comparison with experimental measurements. *Physics of Plasmas*, 25:022305, 2018.
[27] F D Halpern, J L Terry, S J Zweben, B LaBombard, M Podesta, and P Ricci. Comparison of 3D flux-driven scrape-off layer turbulence simulations with gas-puff imaging of Alcator C-Mod inner-wall limited discharges. *Plasma Physics and Controlled Fusion*, 57(5):054005, 2015.
[28] Federico D. Halpern, Brian LaBombard, James L. Terry, and Stewart J. Zweben. Outer midplane scrape-off layer profiles and turbulence in simulations of Alcator C-Mod inner-wall limited discharges. *Physics of Plasmas*, 24(7):072502, 2017.
[29] A N Simakov and P J Catto. *Physics of Plasmas*, 10(12):pp. 4744–4757, December 2003.
[30] B D Dudson et al. *J.Plasma Phys.*, 81(01):365810104, 2015. doi:10.1017/S0022377814000816.
[31] J Leddy and B Dudson. *Plasma Phys. Control. Fusion*, 59:125011, 2017.
[32] J Leddy, B Dudson, and H Willett. *Nucl. Mat. and Energy*, 12:994–998, 2016.
[33] W. Fundamenski, O.E. Garcia, V. Naulin, R.A. Pitts, A.H. Nielsen, J. Juul Rasmussen, J. Horacek, J.P. Graves, and JET EFDA contributors. Dissipative processes in interchange driven scrape-off layer turbulence. *Nuclear Fusion*, 47(5):417–433, 2007.
[34] F. Militello, P. Tamain, W. Fundamenski, A. Kirk, Volker Naulin, and Anders Henry Nielsen. Experimental and numerical characterization of the turbulence in the scrape-off layer of mast. *Plasma Physics and Controlled Fusion*, 55(2):025005, 2013.
[35] Ning Yan, Anders Henry Nielsen, G.S. Xu, Volker Naulin, Jens Juul Rasmussen, Jens Madsen, H. Q. Wang, S. C. Liu, W. Zhang, L. Wang, and B. N. Wan. Statistical characterization of turbulence in the boundary plasma of east. *Plasma Physics and Controlled Fusion*, 55(11):–, 2013.
[36] O.E. Garcia, V. Naulin, A.H. Nielsen, and J. Juul Rasmussen. Turbulence and intermittent

transport at the boundary of magnetized plasmas. *Physics of Plasmas*, 12(6):062309, 2005.
[37] J J Rasmussen et al. *Plasma Phys. Control. Fusion*, 58:014031, 2016.
[38] R Kube and O E Garcia. *Physics of Plasmas*, 22:012502, 2015.
[39] L Wasserman. *All of Statistics*. Springer, 2005.
[40] P J Catto, A N Simakov, F I Parra, and G Kagan. *Plasma Phys. Control. Fusion*, 50:115006, 2008.
[41] M Giacomin and P Ricci. *arXiv*, page 2004.12377, 2020.
[42] C Silva, J Adamek, H Fernandes, and H Figueiredo. Comparison of fluctuations properties measured by langmuir and ball-pen probed in the isttok boundary plasma. *Plasma Phys. Control. Fusion*, 57:025003, 2015.
[43] S Murphy-Sugrue et al. Improved understanding of the ball-pen probe through particle-in-cell simulations. *Plasma Phys. Control. Fusion*, 59:055007, 2017.
[44] C Hidalgo et al. Empirical similarity in the probability density function of turbulent transport in the edge plasma region in fusion plasmas. *Plasma Phys. Control. Fusion*, 44:1557, 2002.
[45] B Ph. van Milligen. Additional evidence for the universality of the probability distribution of turbulent fluctuations and fluxes in the scrape-off layer region of fusion plasmas. *Physics of Plasmas*, 12:052507, 2005.
[46] Frank J. Massey. The kolmogorov-smirnov test for goodness of fit. *Journal of the American Statistical Association*, 46(253):68–78, 1951.
[47] Eric Jones, Travis Oliphant, Pearu Peterson, et al. SciPy: Open source scientific tools for Python, 2001–.
[48] M Giacomin, L.N. Stenger, and P Ricci. Turbulence and flows in the plasma boundary of snowflake magnetic configurations. *Nuclear Fusion*, 60(2):024001, 2020.
[49] N Bisai and P K Kaw. *Physics of Plasmas*, 25:012503, 2018.